

# On sensor fusion for airborne wind energy systems <sup>\*†</sup>

L. Fagiano<sup>‡</sup>, K. Huynh, B. Bamieh, and M. Khammash<sup>§</sup>

## Abstract

A study on filtering aspects of airborne wind energy generators is presented. This class of renewable energy systems aims to convert the aerodynamic forces generated by tethered wings, flying in closed paths transverse to the wind flow, into electricity. The accurate reconstruction of the wing's position, speed and heading is of fundamental importance for the automatic control of this kind of systems. The difficulty of the estimation problem comes from the nonlinear dynamics, wide speed range, large accelerations and fast changes of direction that the wing experiences during operation. It is shown that the overall nonlinear system has a specific structure allowing its partitioning into sub-systems, hence leading to a series of simpler filtering problems. Different sensor setups are then considered, and the related sensor fusion algorithms are presented. The results of experimental tests carried out with a small-scale prototype are discussed. The designed filtering algorithms rely purely on kinematic laws, hence they are independent from features like wing area, aerodynamic efficiency, mass, etc. Therefore, the presented results are representative also of systems with larger size and different wing design, including systems with one and two tethers and/or rigid wings.

## 1 Introduction

High-altitude wind is a vast, still untapped renewable source of energy that has received an increasing attention in the last decade, from both industry and academia, with the ongoing development of a series of technologies that fall under the umbrella name of airborne wind energy. While many concepts of airborne wind energy generators were present already in patents and publications in the late 1970s [21, 16, 19], it is only in recent years that an increasing number of research groups and companies started to develop operating prototypes to convert the energy of high-altitude wind, blowing up to 1000 m from the ground, into electricity (see e.g. [20, 23, 1, 2, 3, 7, 17, 8, 24, 5, 25]). The activities carried out worldwide in the last six years allowed to define and assess, through theoretical, numerical and experimental research, some common grounds of airborne wind energy (see [12] for an overview), as well as its potentials to provide cheap electricity in large quantities, available practically everywhere in the world [13, 15].

Airborne wind energy generators exploit the motion of wings flying fast in the so-called crosswind conditions, i.e. roughly perpendicularly to the wind flow, and linked to the ground by flexible lines. The aerodynamic forces generated by the wing are then converted into electricity using one of several possible approaches [12]. Control engineering plays a crucial role in airborne wind energy technologies, since, differently from conventional wind energy based on wind turbines, there is no passive, rigid structure that constrains the motion of the wing in the air and imposes its crosswind motion. Rather, this task has to be accomplished by an active control system that keeps track of the wing motion and issues suitable control inputs through actuators. In the last six years, the problem of control design for airborne wind energy generators has been studied by several research groups and companies, leading to a quite significant series of theoretical and numerical studies (see e.g. [17, 27, 8, 14, 5, 15]) as well as experimental tests, of which few works in the literature report measured data [8, 13, 11].

All of the mentioned control approaches rely on the availability of a series of variables to be used for feedback, most notably the wing's three-dimensional position and speed. The problem of estimating with sufficient accuracy and limited

<sup>\*</sup>This manuscript is a preprint of a paper submitted for possible publication on the IEEE Transactions on Control Systems Technology and is subject to IEEE Copyright. If accepted, the copy of record will be available at **IEEEExplore** library: <http://ieeexplore.ieee.org/>.

<sup>†</sup>This research has received funding from the California Energy Commission under the EISG grant n. 56983A/10-15 “Autonomous flexible wings for high-altitude wind energy generation”, and from the European Union Seventh Framework Programme (FP7/2007-2013) under grant agreement n. PIOF-GA-2009-252284 - Marie Curie project “Innovative Control, Identification and Estimation Methodologies for Sustainable Energy Technologies”. The authors acknowledge SpeedGoat®’s Greengoat program.

<sup>‡</sup>Corresponding author: fagiano@control.ee.ethz.ch.

<sup>§</sup>The authors are with the Dept. of Mechanical Engineering, University of California at Santa Barbara, CA, USA. L. Fagiano is also with the Automatic Control Laboratory, Swiss Federal Institute of Technology, Zurich, Switzerland. M. Khammash is also with the Department of Biosystems Science and Engineering, Swiss Federal Institute of Technology, Zurich, Switzerland.

lag these quantities is therefore of paramount importance in the field, however in the literature there is a lack of works on this topic, highlighting the specific issues that need to be addressed and providing either numerical or experimental results.

In this paper, we contribute to fill this gap by providing a formulation of the estimation problem and by analyzing two different sensor setups and the related sensor fusion algorithms. In particular, the first sensor setup implies the use of a commercial Inertial Measurement Unit (IMU), installed on the wing and equipped with accelerometers, gyroscopes, magnetometers, GPS, and a barometer. We propose two algorithms for this sensor setup: the first approach is a quite standard linear observer, while the second one introduces a nonlinear correction to account for the specific kinematic constraints of the considered application. In the second sensor setup, we consider the use of a line angle measurement system in addition to the accelerometers, gyroscopes and magnetometers. The presented study is focused on the estimation of the wing's position and of its "speed angle", which is a variable well-suited for automatic control strategies, when the wing is flying fast in crosswind conditions. We present experimental results obtained with a small-scale prototype operating with a fixed line length of about 30 m and equipped with an IMU and a line angle measurement system, which we developed and built ad-hoc for this application. The equations employed in the design of the observer are based purely on kinematics, hence they are exact (i.e. they are not affected by uncertainty in the system's parameters) and independent from system's characteristics like the wing area, aerodynamic efficiency, mass, etc. Therefore, the presented experimental results are representative also of systems with larger wing size and different design, including systems with one and two tethers and/or rigid wings.

## 2 System description, model equations and sensors setup

### 2.1 System description

The considered system is based on a small-scale prototype built at the University of California, Santa Barbara, shown in Fig. 1 (see [4] for a short movie clip). A flexible wing (inflatable power kites are used in the experiments) is linked



Figure 1: Small-scale prototype for the control of tethered wings built at the University of California, Santa Barbara.

by three lines to a ground unit (GU). In normal flight conditions, the wing's trajectory evolves downwind with respect to the GU. The GU is fixed to the ground and it is equipped with actuators, able to influence the wing's path: a human operator or an automatic control algorithm commands the actuators in order to obtain "figure-eight" crosswind paths,

which maximize the generated forces [12]. This paper is devoted to the problem of estimating in real-time, in the described flying conditions, the wing's position as well as its "speed angle" of the wing. In the next section, we provide a formal definition of these variables and we introduce the related notation and model equations.

The prototype operates with a fixed length of the lines of  $r = 30$  m, hence it is not able to generate electricity through the synchronized reeling out of the three lines, as it is typical in ground-based airborne wind energy systems ([12]). Instead, the energy needed for the operation of the system is drawn from batteries installed on the GU. The use of a fixed, short lines' length (as compared with the intended operating conditions of this kind of systems, ranging from 100 to 1000 m of lines' length) does not impair the significance of the presented study, rather it increases it, for at least four reasons: first, airborne wind energy systems operate with very low line unrolling speed as compared with the other components of the wing's speed vector, so the behavior of the wing does not change significantly between fixed line length and variable line length; second, the optimal operation of airborne wind energy generators is obtained with a constant line speed, and the settings considered here can be regarded to as a particular case of such operating conditions, i.e. with constant line speed equal to zero; third, the use of fixed lines' length yields the largest possible forces for given wind conditions, hence the highest accelerations and angular velocities, making the estimation problem more challenging; finally, the use of short lines implies that the wing's path is contained in a small portion of the aerial space, with consequent much more frequent changes of direction and inversions of motion, again increasing the difficulty of the filtering problem.

## 2.2 Model equations

Before stating the model equations used to design our filtering algorithms, we need to introduce a series of right-handed reference systems, as well as the transformations to convert a given vector from one reference to another. A first, inertial

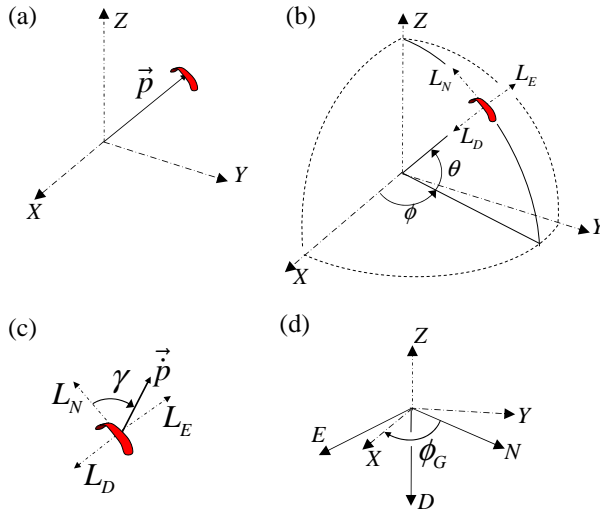


Figure 2: (a) Coordinate system  $G$  and position of the wing  $\vec{p}$ ; (b) local coordinate system  $L = (L_N, L_E, L_D)$  and spherical coordinates  $\theta, \phi$ ; (c) wing speed angle  $\gamma$ ; (d) coordinate systems  $G$  and NED and angle  $\phi_G$ .

coordinate system  $G \doteq (X, Y, Z)$  (Fig. 2-(a)) is centered at the GU location, with the  $X$  axis parallel to the ground, contained in the symmetry plane of the GU and pointing downwind towards the wing. The  $Z$  axis is perpendicular to the ground pointing upwards, and the  $Y$  axis forms a right-handed system. The wing position vector expressed in the reference system  $G$  is denoted by  $\vec{p}_G = [p_X, p_Y, p_Z]^T \in \mathbb{R}^3$ , where  $p_X, p_Y$  and  $p_Z$  are the scalar components of  $\vec{p}_G$  along the axes  $X, Y$  and  $Z$ , respectively, and  $T$  stands for the matrix transpose operation. The wing's position can be also expressed in the spherical coordinates  $\theta, \phi$  (Fig. 2-(b)), where  $\theta \in [0, \frac{\pi}{2}]$  is the angle between the  $(X, Y)$  plane and vector  $\vec{p}_G$  and  $\phi \in [-\pi, \pi]$  is the angle between the  $X$  axis and the projection of  $\vec{p}_G$  onto the  $(X, Y)$  plane, taken to be positive for a positive rotation around the  $Z$  axis. In particular, we have:

$$\vec{p}_G = \begin{bmatrix} p_X \\ p_Y \\ p_Z \end{bmatrix} = r \begin{bmatrix} \cos(\theta) \cos(\phi) \\ \cos(\theta) \sin(\phi) \\ \sin(\theta) \end{bmatrix} \quad (1)$$

where  $r$  is the distance between the GU and the wing, equal to the lines' length in our setup. We note that the angle  $\theta$  considered here is the complement to  $\frac{\pi}{2}$  with respect to the angle employed in previous works (see e.g. [8]), and that the  $\theta, \phi$  angles are different from those used in [11].

Angles  $\theta, \phi$  also define a second, non-inertial Cartesian coordinate system,  $L \doteq (L_N, L_E, L_D)$ , which we call "local". Vector  $\vec{p}_G$  (as well as any other vector) can be expressed in system  $L$  by using the rotation matrix  $R_{G \rightarrow L}$ :

$$\vec{p}_L = R_{G \rightarrow L} \vec{p}_G, \quad (2)$$

$$R_{G \rightarrow L} = \begin{bmatrix} -\sin(\theta)\cos(\phi) & -\sin(\theta)\sin(\phi) & \cos(\theta) \\ -\sin(\phi) & \cos(\phi) & 0 \\ -\cos(\phi)\cos(\theta) & -\sin(\phi)\cos(\theta) & -\sin(\theta) \end{bmatrix}, \quad (3)$$

and the inverse transformation is given by the rotation matrix  $R_{L \rightarrow G} = R_{G \rightarrow L}^{-1} = R_{G \rightarrow L}^T$ . The axes  $L_N$  and  $L_E$  define the tangent plane at point  $\vec{p}_G$  to the sphere of radius  $r$ , on which the wing's trajectory is confined, and they can be interpreted as local north and east direction relative to such a sphere. Hence,  $L_E$  is always parallel to the ground (i.e. to the  $(X, Y)$  plane). The axis  $L_D$  thus represents the local down, pointing from the wing to the center of the sphere (i.e. to the GU location).

We further consider the wing's coordinate system,  $K \doteq (K_x, K_y, K_z)$ , and standard geographical North East Down system,  $NED \doteq (N, E, D)$ . System  $K$  is centered at  $\vec{p}_G$ , it is non-inertial and fixed with respect to the wing, i.e. it provides the wing's orientation. The rotation matrix  $R_{NED \rightarrow G}$  is used to express a vector in  $NED$ -coordinates into  $G$ -coordinates:

$$R_{NED \rightarrow G} = \begin{pmatrix} \cos(\phi_G) & \sin(\phi_G) & 0 \\ \sin(\phi_G) & -\cos(\phi_G) & 0 \\ 0 & 0 & -1 \end{pmatrix}, \quad (4)$$

where  $\phi_G \in [0, 2\pi]$  is the angle between the  $N$  axis and the  $X$  axis, measured by a positive rotation around the  $D$  axis (see Fig. 2-(d)). Moreover, a vector expressed in the  $K$  system can be converted into the  $NED$  system by means of the rotation matrix  $R_{K \rightarrow NED}(q)$ , where  $q = [q_1, q_2, q_3, q_4]^T \in \mathbb{R}^4$  is the quaternion defining the relative orientation between  $K$  and  $NED$  (see e.g. [18, 9]):

$$R_{K \rightarrow NED}(q) = \begin{pmatrix} 2(q_1^2 + q_2^2) - 1 & 2(q_2 q_3 - q_1 q_4) & 2(q_2 q_4 + q_1 q_3) \\ 2(q_2 q_3 + q_1 q_4) & 2(q_1^2 + q_3^2) - 1 & 2(q_3 q_4 - q_1 q_2) \\ 2(q_2 q_4 - q_1 q_3) & 2(q_3 q_4 + q_1 q_2) & 2(q_1^2 + q_4^2) - 1 \end{pmatrix}, \quad (5)$$

The matrix  $R_{K \rightarrow G} \doteq R_{NED \rightarrow G} R_{K \rightarrow NED}$  can be used to express a vector in  $K$  coordinates into  $G$  coordinates. Finally, we define the wing's speed angle  $\gamma \in [-\pi, \pi]$  as follows (see Fig. 2-(c)):

$$\gamma \doteq \arctan_2(\dot{p}_{L_E}, \dot{p}_{L_N}), \quad (6)$$

where  $\arctan_2(\dot{p}_{L_E}, \dot{p}_{L_N}) \in [-\pi, \pi]$  is the 4-quadrant arc tangent function and  $\dot{p}_{L_E}, \dot{p}_{L_N}$  are proportional to the sine and cosine components of  $\gamma$ , respectively. The angle  $\gamma$  provides the angle between the wing's speed vector and the local north axis,  $L_N$ , measured positive for a positive rotation around the local down  $L_D$ . We note that, since the considered system has fixed line length, vector  $\vec{p}$  is always contained in the  $(L_N, L_E)$  plane. In case of variable line length, equation (6) has to be adjusted by considering the projection of  $\vec{p}$  onto  $(L_N, L_E)$ . Angle  $\gamma$  is particularly important as feedback variable for automatic control algorithms, since it can be easily linked to the wing's path: as an example,  $\gamma = 0$ ,  $\gamma = \frac{\pi}{2}$  and  $\gamma = \pi$  indicate that the wing is moving, respectively, towards the local north, parallel to the ground towards the local east, or towards the ground.

We are now in position to introduce the model equations we consider in this work. These equations are based entirely on the system's kinematics, i.e. they are basically obtained by differentiating twice the vector  $\vec{p}_G(t)$  with respect to the time variable  $t$ . Kinematic equations bring two important advantages: 1) they provide an exact model, i.e. there are no neglected dynamics even for flexible wings, and 2) they do not depend on any of the system's characteristics, like mass, shape, moments of inertia and aerodynamics of the wing. Indeed these features influence the motion of the wing through complex, infinite dimensional nonlinear dynamics, whose inputs are the steering command given by the GU and the (unmeasured) wind, yet such dynamics are totally irrelevant for our scope if a measure or estimate of  $\vec{p}_G(t)$  is available. However, while the kinematics in the inertial frame  $G$  are given by linear operators (i.e. derivatives), we still end up with nonlinear model equations, due to the fact that we measure the involved variables in different reference frames. In order

to facilitate the observer design, we split the model into five interconnected subsystems, as shown in Fig. 3. The involved variables are the wing position, speed and acceleration in the reference  $G$ ,  $\vec{p}_G(t)$ ,  $\dot{\vec{p}}_G(t)$ ,  $\ddot{\vec{p}}_G(t)$ , the wing acceleration in the reference  $K$ ,  $\vec{p}_K(t)$ , the quaternion  $q(t)$ , finally the wing angular velocity vector in the reference  $K$ ,  $\vec{\omega}_K(t)$ . The model equations are:

$$\mathcal{L} : \begin{bmatrix} \frac{d\vec{p}_G(t)}{dt} \\ \frac{d\dot{\vec{p}}_G(t)}{dt} \end{bmatrix} = \begin{bmatrix} 0_3 & I_3 \\ 0_3 & 0_3 \end{bmatrix} \begin{bmatrix} \vec{p}_G(t) \\ \dot{\vec{p}}_G(t) \end{bmatrix} + \begin{bmatrix} 0_3 \\ I_3 \end{bmatrix} \vec{p}_G(t) \quad (7a)$$

$$\mathcal{N} : \dot{q}(t) = \frac{1}{2} \begin{bmatrix} 0 & -\omega_{K_x} & -\omega_{K_y} & -\omega_{K_z} \\ \omega_{K_x} & 0 & -\omega_{K_z} & \omega_{K_y} \\ \omega_{K_y} & \omega_{K_z} & 0 & -\omega_{K_x} \\ \omega_{K_z} & -\omega_{K_y} & \omega_{K_x} & 0 \end{bmatrix} \begin{bmatrix} q_1 \\ q_2 \\ q_3 \\ q_4 \end{bmatrix} \quad (7b)$$

$$f_1 : \vec{p}_G(t) = R_{NED \rightarrow G}(\phi_G) R_{K \rightarrow NED}(q(t)) \vec{p}_K(t) \quad (7c)$$

$$f_2 : \begin{cases} \theta(t) = \arcsin\left(\frac{p_Z(t)}{r}\right) \\ \phi(t) = \arctan\left(\frac{p_Y(t)}{p_X(t)}\right) \end{cases} \quad (7d)$$

$$f_3 : \begin{cases} \vec{p}_L = R_{G \rightarrow L} \vec{p}_G \\ \gamma(t) = \arctan_2(\dot{p}_{L_E}(t), \dot{p}_{L_N}(t)) \end{cases} \quad (7e)$$

where  $0_3$  is a  $3 \times 3$  matrix of zeros, and  $I_3$  is the  $3 \times 3$  identity matrix. Thus, the considered model has  $\vec{p}_K$ ,  $\vec{\omega}_K(t)$  as inputs

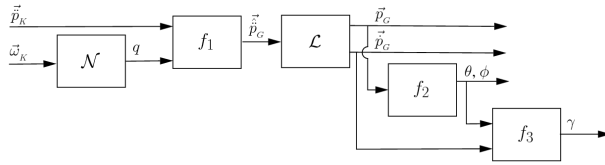


Figure 3: Scheme of the considered kinematic model.

and  $\vec{p}_G(t)$ ,  $\dot{\vec{p}}_G(t)$ ,  $q(t)$  as states, and it is composed by a linear dynamical system,  $\mathcal{L}$ , a nonlinear one,  $\mathcal{N}$ , and three static nonlinear functions,  $f_1$ ,  $f_2$ ,  $f_3$ . The only involved parameters are the constant angle  $\phi_G$ , giving the orientation of the GU with respect to the geographical north, and the length  $r$  of the lines. Both these parameters can be measured accurately and are assumed to be known exactly here. In the next section, we will describe the different considered sensor setups and indicate the corresponding measured variables.

## 2.3 Sensors setup

Several sensors are installed on the GU and onboard the wing, giving a range of different possibilities for the design of observers for  $\vec{p}_G(t)$ ,  $\dot{\vec{p}}_G(t)$ , and  $\gamma(t)$ . A GPS and three magnetometers are installed on the GU, providing its geographical location in  $NED$  as well as the angle  $\phi_G$ . Moreover, the GU is equipped with a line angle measurement system (shown in Fig. 4), which provides a direct measurement of the angle of the main line connecting the wing to the GU. This sensor has been developed and built ad-hoc for this application and it employs two incremental encoders. The encoders are connected to the center line via a metal rod and a small pulley which allow the center line to slide with low friction with respect to the rod while the wing is flying. The first encoder measures the angle between the metal rod and the  $(X, Y)$  plane, while the second one measures the angle between the  $X$  axis and the projection of the metal rod onto  $(X, Y)$ . Both encoders have a resolution of  $\frac{2\pi}{400}$  rad, i.e. 400 counts for each full revolution. Driven by the movement of the center line, the metal rod rotates following the wing's path, and the encoders measure such rotations in terms of the above mentioned angles. More specifically, the readings from the two incremental encoders, denoted as  $\theta_B$  and  $\phi_B$ , can be converted into



Figure 4: Line angle sensor

measurements of  $\theta$  and  $\phi$  via the following equations (see Fig. 5):

$$L = \sqrt{L_1^2 + L_2^2} \quad (8a)$$

$$\theta'_B = \theta_B - \arctan_2\left(\frac{L_1}{L_2}\right) \quad (8b)$$

$$l'_1 = L \sin(\theta'_B) \quad (8c)$$

$$l'_2 = L \cos(\theta'_B) \cos(\phi_B) - l_2 \quad (8d)$$

$$l'_3 = L \cos(\theta'_B) \sin(\phi_B) \quad (8e)$$

$$\theta = \arctan\left(\frac{l'_1 + l_1}{\sqrt{l'_2^2 + l'_3^2}}\right) \quad (8f)$$

$$\phi = \arctan_2(l'_3, l'_2), \quad (8g)$$

where  $L_1$  and  $L_2$  are, respectively, the lengths of the metal rod and the pulley on top of it, and  $l_1$ ,  $l_2$  are the distances between the encoders' position  $P_2$  and the attachment point of the center line on the GU,  $P_1$ . All quantities  $L_1$ ,  $L_2$ ,  $l_1$ ,  $l_2$  are fixed and known.

As regards onboard sensors, the wing is equipped with an Inertial Measurement Unit (IMU) manufactured by SBG Systems®, comprising three accelerometers, three gyroscopes, three magnetometers, a barometer, and a GPS. A 900 MHz radio is also installed on the wing and transmits the measurements collected by the IMU to a receiver on the GU, at a rate of 115200 Baud. The accelerometers have a measurement range of  $\pm 5$  g (where g is the gravity constant) and noise density of  $2.5 \times 10^{-4}$  g/ $\sqrt{\text{Hz}}$ . The gyroscopes have a measurement range of  $\pm 300^\circ/\text{s}$  and noise density of  $0.05^\circ/(\text{s}\sqrt{\text{Hz}})$ . The magnetometers have a measurement range of  $\pm 1.2$  Gauss and noise density of  $1 10^{-5} \times \text{Gauss}/\sqrt{\text{Hz}}$ . The barometer provides a measurement of barometric altitude with a resolution of 20 cm. All sensors mentioned so far provide a new measurement with a sampling time of  $T_s = 0.02$  s. Finally, the onboard GPS has a nominal horizontal accuracy (i.e. on the ( $N, E$ ) plane) of  $\pm 2.5$  m and a sampling time of 0.25 s.

In the following, we will implicitly assume that:

- the line angle sensor provides a measure of the  $\theta$ ,  $\phi$  angles;
- the position measured by the onboard GPS coincides with  $\vec{p}_G$ ;
- the barometer provides a measure of  $p_Z$ ;
- the IMU is fixed with respect to the kite, hence the accelerometers, gyroscopes and magnetometers provide measurement of, respectively,  $\vec{p}_K$ ,  $\vec{\omega}_K$ , and  $q$ .

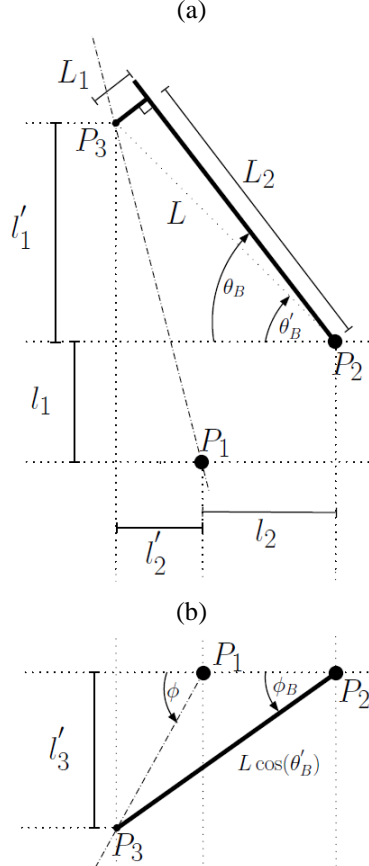


Figure 5: Diagram of the line angle sensor: (a) side view and (b) top view. Dash-dotted line: center line of the wing; thick solid lines: metal rod and pulley linking the encoders to the center line.

These assumptions imply that the wing's lines are parallel to its position vector  $\vec{p}_G$ , that the position of the IMU coincides with  $\vec{p}_G$  and that the IMU itself is fixed to the wing, so that the measured accelerations and angular speeds corresponds to those of the wing. Given, the short length of the wing's lines, such hypotheses are reasonable in the considered application.

### 3 Sensor Fusion for Airborne Wind Energy

In this section we present different algorithms to estimate the wing's position and speed angle,  $\vec{p}_G(t)$  and  $\gamma(t)$ . In the following, we use the notation “~” to indicate the noise-corrupted measurement of a given variable, e.g.  $\vec{p}_G$  is the measurement of the position vector seen from system  $G$ ,  $\vec{p}_G$ . Moreover, we indicate with “^” the estimated variables, i.e. the output of the observer.

As a first step, we exploit the structure of the considered kinematic model to separate the problem of estimating the wing orientation (i.e. the quaternion  $q(t)$ ) from the one of estimating its position and speed. In fact, since the nonlinear system  $\mathcal{N}$  is known and the IMU provides a measurement of both its input and its state, i.e.  $\vec{\omega}_K(t)$  and  $\tilde{q}(t)$ , an extended Kalman filter (EKF) approach can be adopted to obtain the value of  $\hat{q}(t)$ . The use of EKFs for the absolute orientation of rigid bodies using gyroscopes and magnetometers has been already studied in the literature (see e.g. [22]), and the IMU employed in this study already includes its own EKF for this purpose. We indicate such a filter as  $\mathcal{N}_{EKF}$ . With the estimate  $\hat{q}(t)$  provided by  $\mathcal{N}_{EKF}$ , we can then compute the rotation matrix  $R_{K \rightarrow NED}(\hat{q}(t))$  by using (5). Then, we

compute an estimate  $\hat{\vec{p}}_G(t)$  of  $\vec{p}_G(t)$  through the static nonlinear function  $\hat{f}_1$  given by:

$$\hat{f}_1 : \hat{\vec{p}}_G(t) = R_{NED \rightarrow G}(\phi_G)R_{K \rightarrow NED}(\hat{q})\vec{p}_K(t) + \begin{bmatrix} 0 \\ 0 \\ g \end{bmatrix}. \quad (9)$$

$\hat{f}_1$  is obtained from  $f_1$  (7c) by using the estimated rotation matrix  $R_{K \rightarrow NED}(\hat{q}(t))$  instead of the “true” one, and then by removing the bias given by the gravity acceleration  $g$ . The latter is present in our setup due to the characteristics of the employed MEMS accelerometers. The approach described so far is used as a preliminary step for any of the observers described in the following sections, whose goal is to estimate the wing’s position and speed. In particular, consider that the estimate  $\hat{\vec{p}}_G(t)$  can be re-written as:

$$\hat{\vec{p}}_G(t) = \vec{p}_G(t) + \vec{\eta}_p(t), \quad (10)$$

where  $\vec{\eta}_p(t) \in \mathbb{R}^3$  is some estimation error that we consider as process noise. Then, the estimate  $\hat{\vec{p}}_G(t)$  can be regarded to as a noise-corrupted input for the linear system  $\mathcal{L}$  (see Fig. 3). Following this idea, we will use a steady-state Kalman filter, based on  $\mathcal{L}$ , to compute  $\vec{p}_G(k)$  and  $\hat{\vec{p}}_G(k)$ . In order to do so, we discretize  $\mathcal{L}$  by forward difference with the employed sampling time  $T_s$ :

$$\begin{aligned} \begin{bmatrix} \vec{p}_G(k+1) \\ \vec{p}_G(k+1) \end{bmatrix} &= \underbrace{\begin{bmatrix} I_3 & T_s I_3 \\ 0_3 & I_3 \end{bmatrix}}_A \begin{bmatrix} \vec{p}_G(k) \\ \vec{p}_G(k) \end{bmatrix} + \underbrace{\begin{bmatrix} 0_3 \\ T_s I_3 \end{bmatrix}}_B \vec{p}_G(k) + \vec{\eta}_p(k) \\ \vec{p}_G(k) &= \underbrace{\begin{bmatrix} I_3 & 0_3 \end{bmatrix}}_C \begin{bmatrix} \vec{p}_G(k) \\ \hat{\vec{p}}_G(k) \end{bmatrix} + \vec{\eta}_m(k), \end{aligned} \quad (11)$$

where  $k \in \mathbb{Z}$  is the discrete time variable and  $\vec{\eta}_m \in \mathbb{R}^3$  represents the measurement noise. In classical Kalman filtering theory,  $\vec{\eta}_p$  and  $\vec{\eta}_m$  are assumed to be independent white Gaussian processes with covariance matrices  $Q$  and  $R$ , respectively [26]. Here, the measurement and process noises can be reasonably assumed to be independent, since they pertain to completely different sensors (accelerometers, gyroscopes and magnetometers for the input  $\hat{\vec{p}}_G(k)$  and either GPS and barometer or line angle sensor for the output  $\vec{p}_G(k)$ ), yet they are not white Gaussian processes, since the measurements are the result of algorithms like  $\mathcal{N}_{EKF}$  or the GPS algorithm. However, the matrices  $Q$  and  $R$  can still be used as tuning knobs in the design of the linear observer: a larger  $Q$  with respect to  $R$  will yield an observer that relies more on the measured output and carries out more aggressive corrections of the estimates, viceversa a larger  $R$  will yield a smoother course of the estimated variables, with higher discrepancy between the measured and estimated outputs.

The steady-state discrete Kalman Filter is then obtained by the following equations [26, 6]:

Time update ("Predict"):

$$\begin{bmatrix} \hat{\vec{p}}_G^-(k) \\ \hat{\vec{p}}_G^-(k) \end{bmatrix} = A \begin{bmatrix} \hat{\vec{p}}_G^-(k-1) \\ \hat{\vec{p}}_G^-(k-1) \end{bmatrix} + B \hat{\vec{p}}_G(k) \quad (12)$$

Measurement Update ("Correct"):

$$\begin{bmatrix} \vec{p}_G(k) \\ \hat{\vec{p}}_G(k) \end{bmatrix} = \begin{bmatrix} \vec{p}_G^-(k) \\ \hat{\vec{p}}_G^-(k) \end{bmatrix} + K \left( \vec{p}_G(k) - C \begin{bmatrix} \vec{p}_G^-(k) \\ \hat{\vec{p}}_G^-(k) \end{bmatrix} \right) \quad (13)$$

where  $\vec{p}_G^-(k)$ ,  $\hat{\vec{p}}_G^-(k)$  are the a-priori state estimates at step  $k$  given the knowledge of the process prior to step  $k$ , while  $\vec{p}_G(k)$ ,  $\hat{\vec{p}}_G(k)$  are the a-posteriori state estimates at step  $k$  given the knowledge of the measurement  $\vec{p}_G(k)$ . The steady-state Kalman gain  $K$  is computed off-line as:

$$K = AP_\infty C^T (CP_\infty C^T + R)^{-1}, \quad (14)$$

where  $P_\infty$  satisfies the following Algebraic Riccati Equation:

$$P_\infty = AP_\infty A^T - AP_\infty C^T (CP_\infty C^T + R)^{-1} CP_\infty A^T + Q. \quad (15)$$

We will now describe the three different approaches considered in this study. All three of them employ the described procedure to obtain  $\hat{\vec{p}}_G(k)$  and then the Kalman filter (12)-(13) to estimate position and speed, but they use different strategies and sensors to obtain the position measurement  $\vec{p}_G(k)$ . A scheme of each of the three approaches is shown in Fig. 6, where we indicate the Kalman filter as  $\mathcal{L}_{KF}$ .

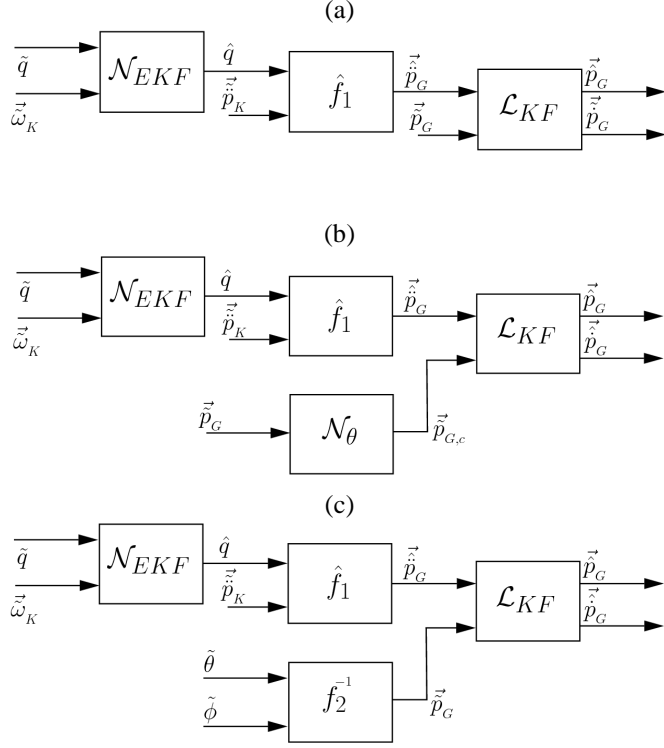


Figure 6: Schemes of the designed observers for the first, second and third approach ((a), (b) and (c), respectively).

### 3.1 First approach: GPS and barometer

We design a first observer (Fig. 6-(a)) by using the GPS to obtain the measurements  $\tilde{p}_X$ ,  $\tilde{p}_Y$ , and the barometer for  $\tilde{p}_Z$ . Hence, the two sensors together provide the position measurement  $\tilde{\vec{p}}_G(k)$  to be used with the Kalman filter (12)-(13). While the GPS can also provide a measurement of the altitude, the related error (about  $\pm 50$  m in our setup) is too large to be used in the considered application. The barometer, on the other hand, is quite accurate provided that an initial tuning procedure is carried out for each test to remove the bias induced by the changing weather conditions. The GPS measurements are obtained by computing the difference of the readings between the onboard GPS and the one placed on the GU. Since the accelerometers have a sampling frequency of 50 Hz, while the GPS provides measurements at a 4 Hz rate, we use a multi-rate Kalman filter in this first approach, which consists in performing the time update (12) at each sampling time of  $T_s = 0.02$  s, and the measurement update (13) every 0.25 s, i.e. when the new GPS measurement is available.

### 3.2 Second approach: GPS and barometer with geometric correction

The filter designed in the second approach employs the same sensors as the previous one, but it also carries out a correction of the measured position on the  $(X, Y)$  plane given by the GPS. Such a correction is based on two observations: 1) the wing motion is constrained on a sphere of known radius  $r$ , 2) the measurements  $\tilde{p}_X$ ,  $\tilde{p}_Y$  given by the GPS are less reliable than the measurement  $\tilde{p}_Z$  provided by the barometer. Using  $\tilde{Z}$ , by inverting (7d) we compute a measure  $\tilde{\theta}$  of angle  $\theta$ , then, we correct  $\tilde{p}_X$ ,  $\tilde{p}_Y$  by re-scaling them in order to match with the line length  $r$  projected onto  $(X, Y)$ , i.e.  $r \cos(\tilde{\theta})$  (compare (1) and Fig. 2-(b)):

$$\begin{aligned}\tilde{p}_{X,c} &= \tilde{p}_X \frac{r \cos(\tilde{\theta})}{\sqrt{\tilde{p}_X^2 + \tilde{p}_Y^2}} \\ \tilde{p}_{Y,c} &= \tilde{p}_Y \frac{r \cos(\tilde{\theta})}{\sqrt{\tilde{p}_X^2 + \tilde{p}_Y^2}}\end{aligned}\tag{16}$$

Then, we use the vector  $\tilde{\vec{p}}_{G,c} = [\tilde{p}_{X,c}, \tilde{p}_{Y,c}, \tilde{p}_Z]^T$  as position measurement for the multi-rate Kalman filter. This second approach is shown in Fig. 6-(b), where the correction (16) is indicated as  $\mathcal{N}_\theta$ .

### 3.3 Third approach: Line angle sensor

The third observer we consider (Fig. 6-(c)) employs the line angle sensor to obtain the position measurement. Hence, in this approach we move away from using the GPS and barometer measurements. By inverting (7d) we have:

$$\begin{aligned}\tilde{p}_X(k) &= r \cos(\tilde{\theta}(k)) \cos(\tilde{\phi}(k)) \\ \tilde{p}_Y(k) &= r \cos(\tilde{\theta}(k)) \sin(\tilde{\phi}(k)) \\ \tilde{p}_Z(k) &= r \sin(\tilde{\theta}(k)),\end{aligned}\quad (17)$$

where  $\tilde{\theta}(k)$ ,  $\tilde{\phi}(k)$  are the measurements provided at 50 Hz by the line angle sensor. Due to the use of incremental encoders, the measurement noise on  $\tilde{\theta}(k)$ ,  $\tilde{\phi}(k)$  is basically given just by the quantization error resulting from the encoders' resolution, i.e.  $\pm \frac{\pi}{400}$  rad.

### 3.4 $\gamma$ filter

In order to obtain an estimate of the speed angle  $\gamma$  (6), we first use (7d) to obtain the angles  $\hat{\theta}$ ,  $\hat{\phi}$  from the filtered position  $\vec{p}_G$ . The latter is obtained, together with the speed estimate  $\hat{\vec{p}}_G$ , using one of the observers presented in the previous sections. Then, we estimate the rotation matrix  $R_{G \rightarrow L}(\hat{\theta}, \hat{\phi})$  by using (3), and we compute an estimate of the speed vector in the  $L$  frame,  $\hat{\vec{p}}_L$ , as:

$$\hat{\vec{p}}_L = R_{G \rightarrow L}(\hat{\theta}, \hat{\phi}) \hat{\vec{p}}_G. \quad (18)$$

Using  $\hat{\vec{p}}_L$ , we compute a first “measurement”  $\tilde{\gamma} \simeq \gamma$  by simply applying its definition (6). However,  $\tilde{\gamma}$  results to be affected by high-frequency oscillations (see section 4 for an example with experimental data), hence it is not suitable to be used for feedback control. In order to have a smooth estimate, we design another observer based on the following state-space model:

$$\begin{aligned}\begin{bmatrix} \dot{\gamma}(k+1) \\ \ddot{\gamma}(k+1) \end{bmatrix} &= \underbrace{\begin{bmatrix} 1 & T_s \\ 0 & 1 \end{bmatrix}}_A \begin{bmatrix} \gamma(k) \\ \dot{\gamma}(k) \end{bmatrix} \\ \tilde{\gamma}(k) &= \underbrace{\begin{bmatrix} 1 & 0 \end{bmatrix}}_C \begin{bmatrix} \gamma(k) \\ \dot{\gamma}(k) \end{bmatrix}.\end{aligned}\quad (19)$$

In particular, we design a standard Luenberger observer [10] to obtain the estimates  $\hat{\gamma}$  and  $\dot{\hat{\gamma}}$ .

Clearly, the three different approaches to estimate the wing's position and speed yield estimates of  $\gamma$  with different accuracy. In the next section, we discuss the performance obtained with the considered filters in experimental tests.

## 4 Experimental results

We designed three different observers for  $\vec{p}_G$ , according to the approaches described in section 3, and consequently three observers for  $\hat{\gamma}$ . In this section, we use the superscripts <sup>1</sup>, <sup>2</sup>, <sup>3</sup> to indicate the filtered position obtained with the approach of section 3.1, 3.2 and 3.3, respectively. For the first and second approach, we used the following covariance matrices:

$$R = \begin{bmatrix} 5 & 0 & 0 \\ 0 & 5 & 0 \\ 0 & 0 & 5 \end{bmatrix} \quad Q = \begin{bmatrix} 50 & 0 & 0 \\ 0 & 50 & 0 \\ 0 & 0 & 50 \end{bmatrix}$$

while for the third approach we used:

$$R = \begin{bmatrix} 0.1 & 0 & 0 \\ 0 & 0.1 & 0 \\ 0 & 0 & 0.1 \end{bmatrix} \quad Q = \begin{bmatrix} 50 & 0 & 0 \\ 0 & 50 & 0 \\ 0 & 0 & 50 \end{bmatrix}$$

The gain for the Luenberger observer used to estimate  $\gamma$  is equal to  $K_\gamma = [0.06, 0.6]^T$ . The length of the lines is  $r = 30$  m. We employed different wings in the experiments, in order to demonstrate that the proposed approach is independent from system's features like wing area, mass, efficiency, etc. In particular, we used three different Airush One® inflatable power

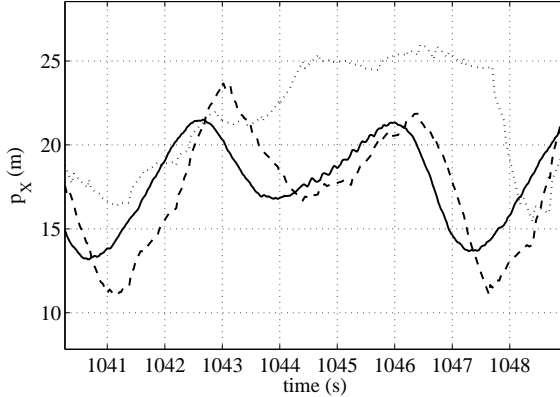


Figure 7: Experimental results. Estimates of the position along the  $X$  axis,  $p_X(t)$ , obtained with the first (dotted line), second (dashed) and third (solid) approaches.

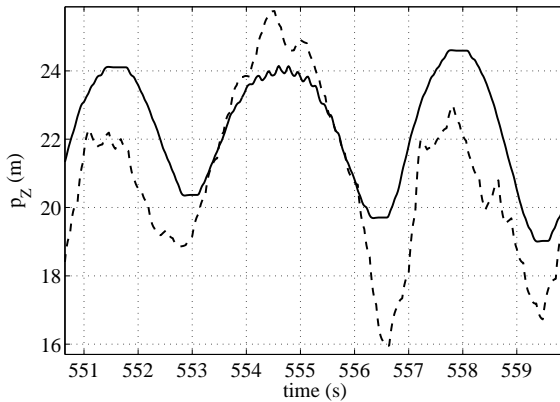


Figure 8: Experimental results. Estimates of the position along the  $Z$  axis,  $p_Z(t)$ , obtained with either the first and second (dashed line) or the third (solid) approach.

kites, with  $12 \text{ m}^2$ ,  $9 \text{ m}^2$  and  $6 \text{ m}^2$  area.

The third approach results to be the most accurate one, thanks to the use of the line angle sensor, which practically yields exact position readings. Hence, in this section we take the estimates  $\hat{p}_G^3$  and  $\hat{\gamma}^3$ , obtained with the third approach, as “true values” and we evaluate the deviations resulting from the first two approaches with respect to the third one. An example of the courses of the position component along the  $X$  axis,  $\hat{p}_X$ , is shown in Fig. 7. It can be noted that the error between  $\hat{p}_X^1$ ,  $\hat{p}_X^2$  and  $\hat{p}_X^3$  can be quite high (of the order of 10 m), with  $\hat{p}_X^2$  being generally better than  $\hat{p}_X^1$ . This shows that the correction (16) we introduced in the second approach indeed improves the estimate with respect to using the plain GPS reading. Moreover, both  $\hat{p}_X^1$  and  $\hat{p}_X^2$  are affected by some delay with respect to  $\hat{p}_X^3$ . The estimates of vertical position result to be more accurate thanks to the use of the barometric altitude instead of the GPS, see Fig. 8 for an example (we note that for the vertical position  $p_Z$ , the first two approaches are equivalent hence resulting in the same filtered values). Table 1 shows the root mean square errors (RMSE) between the first two approaches and the third one, for all of the estimated variables. The results of Table 1 account for about 5 hours of operation at different wind speeds. Considering that a single figure-eight loop has a period of 5-6 seconds, the data in the table correspond to about 3300 complete figure-eight paths. The results in the table confirm that the second approach is generally better than the first one in estimating the wing’s position, especially at larger wind speeds (see Table 1 for 3.5 m/s and above), while the two give similar errors on the  $\gamma$  estimates, which deviate significantly from the third approach. Moreover, it can be noted that the accuracy of the first two approaches get worse as the wind speed is higher. Since the wing’s speed depends linearly on the wind speed (see e.g. [14]), this results indicate that the GPS performance get worse as the wing movements get faster and changes of direction are more frequent. Indeed the provided GPS accuracy ( $\pm 2.5 \text{ m}$  in the  $(N, E)$  plane) is valid for steady state conditions only.

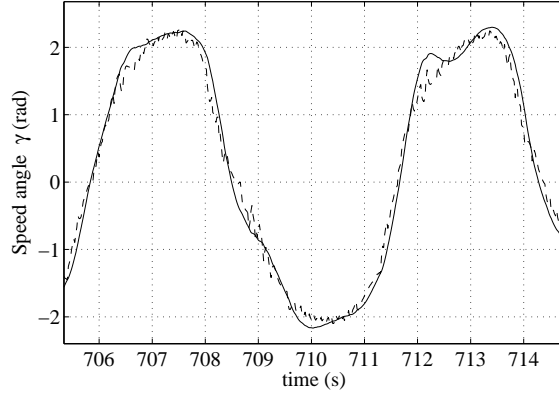


Figure 9: Experimental results. Courses of  $\tilde{\gamma}(t)$  (dashed line) and  $\hat{\gamma}(t)$  obtained with the third approach. Wing area: 12 m<sup>2</sup>.

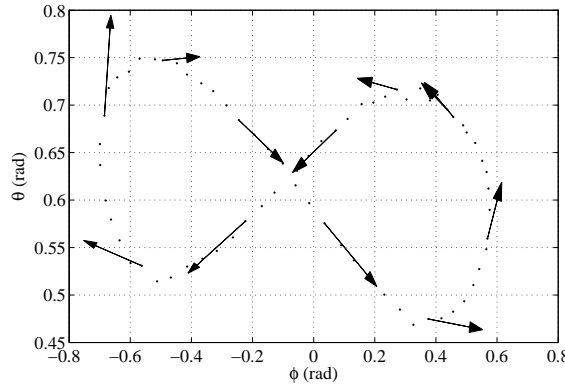


Figure 10: Experimental results. Path of the wing during one figure-eight cycle in the  $(\phi, \theta)$  plane (dotted lines) and gradients obtained with the estimated speed angle  $\hat{\gamma}(t)$  obtained with the third approach (arrows). Wing area: 12 m<sup>2</sup>.

Fig. 9 shows, relative to the third approach, the smoothing effect obtained with the Luenberger observer for the  $\hat{\gamma}^3$  angle with respect to the values of  $\tilde{\gamma}^3$ . A typical example of figure-eight path in the  $(\phi, \theta)$  plane, obtained during the tests, is shown in Fig. 10, together with the gradient vectors  $[\dot{\phi}, \dot{\theta}]^T$  estimated using the values of  $\hat{\gamma}^3$ : it can be noted that the estimated speed angle is quite accurate, with the gradient being almost always tangent to the wing's flying path. The length of the arrows in Fig. 10 is proportional to the wing's speed with respect to the ground. Similar good results have been obtained with all the three different wings, and in different wind conditions (see Fig. 11 for some examples), hence showing the robustness of the approach deriving from the use of kinematic equations to design the filters. These features make the use of the proposed approach and of  $\hat{\gamma}^3$  most suited for feedback control, see [4] for a short movie clip concerned with autonomous flights carried out using such estimation algorithm.

Table 1: Experimental results. Root mean square errors between the estimates obtained with either the first or second approach and the third one.

	Wind speed range (m/s)																					
	1.0-1.5		1.5-2.0		2.0-2.5		2.5-3.0		3.0-3.5		3.5-4.0		4.0-4.5		4.5-5.0		5.0-5.5		5.5-6.0		6.0-6.5	
Approach	1 <sup>st</sup>	2 <sup>nd</sup>	1 <sup>st</sup>	2 <sup>nd</sup>	1 <sup>st</sup>	2 <sup>nd</sup>	1 <sup>st</sup>	2 <sup>nd</sup>	1 <sup>st</sup>	2 <sup>nd</sup>	1 <sup>st</sup>	2 <sup>nd</sup>	1 <sup>st</sup>	2 <sup>nd</sup>	1 <sup>st</sup>	2 <sup>nd</sup>	1 <sup>st</sup>	2 <sup>nd</sup>	1 <sup>st</sup>	2 <sup>nd</sup>	1 <sup>st</sup>	2 <sup>nd</sup>
$p_X$ (m)	5.61	2.36	7.74	5.07	10.67	6.64	12.81	6.96	13.30	7.80	17.18	9.71	28.91	12.45	47.21	14.50	55.39	14.55	56.61	14.93	56.39	15.23
$p_Y$ (m)	7.28	4.16	10.32	10.16	14.18	12.56	12.77	11.16	13.27	10.71	14.97	10.98	18.02	11.12	16.47	10.31	13.35	9.45	12.83	9.61	13.46	9.81
$p_Z$ (m)	0.74	0.74	1.71	1.71	2.13	2.13	2.75	2.75	3.47	3.47	4.58	4.58	6.36	6.36	8.44	8.44	9.30	9.30	9.15	9.15	9.32	9.32
$\gamma$ (rad)	1.70	0.80	1.35	1.44	1.52	1.71	1.50	1.61	1.54	1.72	1.71	1.97	1.90	2.32	2.40	2.37	2.67	2.24	2.65	2.35	2.96	2.39

## 5 Conclusions

We presented a study on the problem of sensor fusion for airborne wind energy systems. We designed three algorithms to estimate the wing's position and speed angle, using different sensors, and we applied them in experimental tests. The presented results allowed to draw some conclusions on the efficacy of the different employed sensors for this kind of application: for relatively short line length, GPS sensors are not suited to track the highly dynamical movement and frequent change of direction of the wing, while line angle sensors results to be very effective. This situation is likely to change for longer line length and larger paths, when the wing keeps a constant heading for longer time: in this context, the GPS performance should improve, while the line angle measurement might be less accurate due to eventual line sag. More expensive GPS sensors and differential GPS systems should also be able to obtain better performance, although for short line length the accuracy and bandwidth of a line angle sensor cannot be matched. The presented algorithms are based on a kinematic model of the system, which is exact and independent from the features of the particular employed wing. Hence, the obtained results are significant also for other wing sizes and for rigid wings.

## References

- [1] Ampyx power website, <http://www.ampyxpower.com/>.
- [2] Windlift website, <http://www.windlift.com/>.
- [3] Kitenergy website, <http://www.kitenergy.net/>.
- [4] EISG project “Autonomous flexible wings for high-altitude wind energy generation”, experimental test movie, August 2012. Available on-line: [http://lorenzofagiano.altervista.org/movies/EISG\\_UCSB\\_auto\\_wing.mp4](http://lorenzofagiano.altervista.org/movies/EISG_UCSB_auto_wing.mp4).
- [5] J. H. Baayen and W. J. Ockels. Tracking control with adaption of kites. *IET Control Theory and Applications*, 6(2):182–191, 2012.
- [6] Yaakov Bar-Shalom, X. Rong Li, and Thiagalingam Kirubarajan. *Estimation and Tracking: Principles, Techniques, and Software*. Artec House, Inc., New York, 1993.
- [7] M. Canale, L. Fagiano, and M. Milanese. Power kites for wind energy generation. *IEEE Control Systems Magazine*, 27(6):25–38, December 2007.
- [8] M. Canale, L. Fagiano, and M. Milanese. High altitude wind energy generation using controlled power kites. *IEEE Transactions on Control Systems Technology*, 18(2):279 –293, mar. 2010.
- [9] Evangelos A. Coutsias and Louis Romero. The quaternions with an application to rigid body dynamics. Technical Report SAND2004-0153, Sandia National Laboratories, 2004.
- [10] G. Ellis. *Observers in Control Systems: A Practical Guide*. Academic Press, San Diego, USA, 2002.
- [11] Michael Erhard and Hans Strauch. Control of towing kites for seagoing vessels. *arXiv*, abs/1202.3641, 2012.
- [12] L. Fagiano and M. Milanese. Airborne wind energy: an overview. In *American Control Conference 2012*, pages 3132–3143, Montreal, Canada, 2012.
- [13] L. Fagiano, M. Milanese, and D. Piga. High-altitude wind power generation. *IEEE Transactions on Energy Conversion*, 25(1):168 –180, mar. 2010.
- [14] L. Fagiano, M. Milanese, and D. Piga. Optimization of airborne wind energy generators. *International Journal of Robust and Nonlinear Controll*, 2011. In press, early view available. doi: 10.1002/rnc.1808.
- [15] Lorenzo Fagiano. *Control of Tethered Airfoils for High-Altitude Wind Energy Generation*. PhD thesis, Politecnico di Torino, Italy, February 2009. Available on-line: [http://lorenzofagiano.altervista.org/docs/PhD\\_thesis\\_Fagiano\\_Final.pdf](http://lorenzofagiano.altervista.org/docs/PhD_thesis_Fagiano_Final.pdf).
- [16] C. A. J. Fletcher and B. W. Roberts. Electricity generation from jet-streams winds. *Journal of Energy*, 3:241–249, 1979.

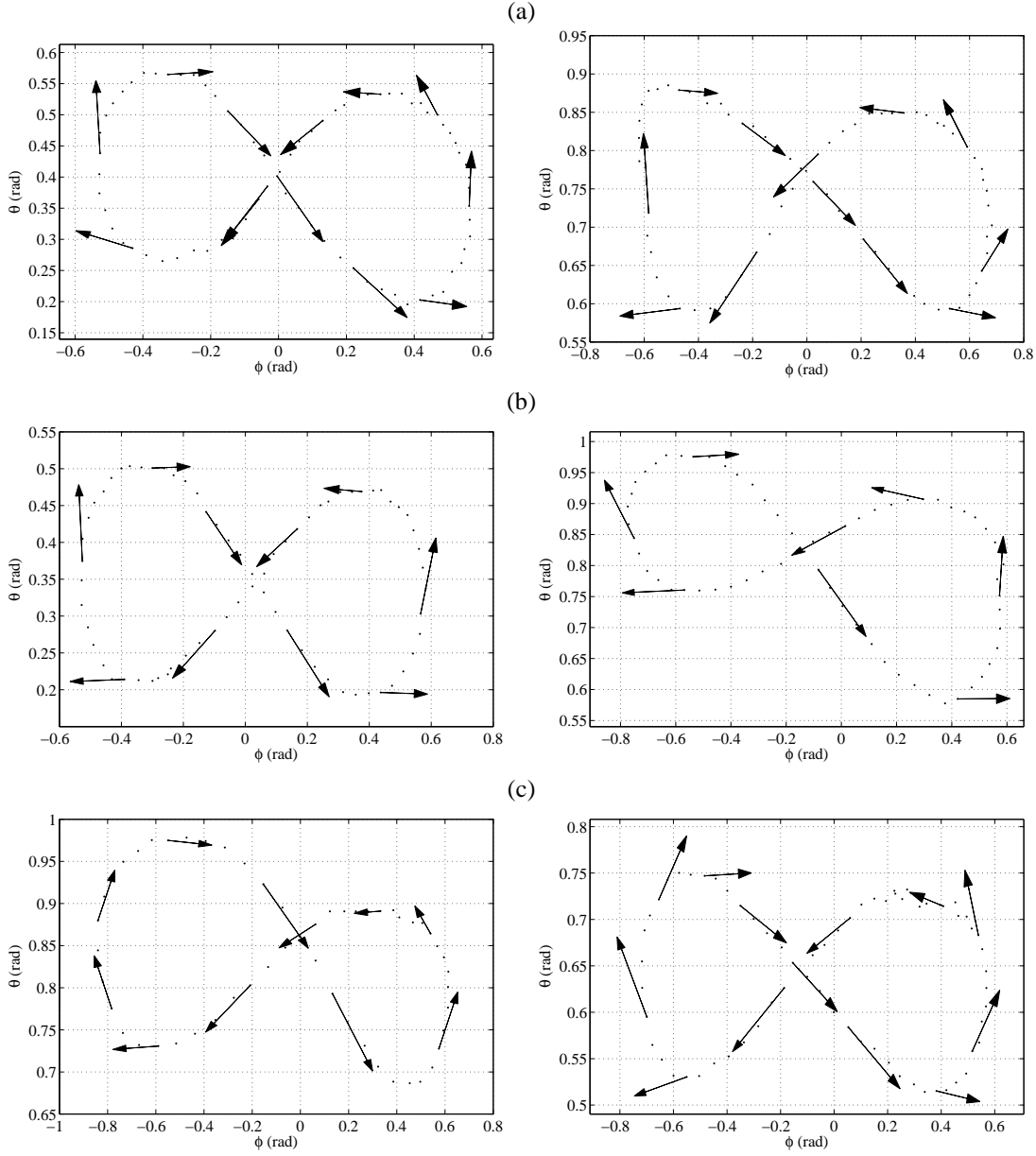


Figure 11: Experimental results. Examples of wing paths (dotted lines) and related gradients (arrows) obtained with the (a)  $6 \text{ m}^2$ , (b)  $9 \text{ m}^2$  and (c)  $12 \text{ m}^2$  wings and with about  $2 \text{ m/s}$  (left) and  $4 \text{ m/s}$  (right) wind speed.

- [17] A. Ilzhöfer, B. Houska, and M. Diehl. Nonlinear MPC of kites under varying wind conditions for a new class of large-scale wind power generators. *International Journal of Robust and Nonlinear Control*, 17:1590–1599, 2007.
- [18] Steven M. LaValle. *Planning Algorithms*. Cambridge University Press, Illinois, US, 2006.
- [19] M. L. Loyd. Crosswind kite power. *Journal of Energy*, 4(3):106–111, 1980.
- [20] Makani Power Inc. <http://www.makanipower.com>.
- [21] M. S. Manalis. Airborne windmills and communication aerostats. *Journal of Aircraft*, 13(7):543–544, 1976.
- [22] Angelo Maria Sabatini. Kalman-filter-based orientation determination using inertial/magnetic sensors: Observability analysis and performance evaluation. *Sensors*, 11(10):9182–9206, September 2011.

- [23] SkySails GmbH & Co., 2010. <http://www.skysails.info>.
- [24] E.J. Terink, J. Breukels, R. Schmehl, and W.J. Ockels. Flight dynamics and stability of a tethered inflatable kiteplane. *AIAA Journal of Aircraft*, 48(2):503–513, 2011.
- [25] C. Vermillion, T. Grunnagle, and I. Kolmanovsky. Modeling and control design for a prototype lighter-than-air wind energy system. In *American Control Conference 2012*, Montreal, Canada, 2012.
- [26] Greg Welch and Gary Bishop. *An Introduction to the Kalman Filter*. ACM, Inc., Chapel Hill, NC, 2001.
- [27] P. Williams, B. Lansdorp, and W. Ockels. Optimal crosswind towing and power generation with tethered kites. *Journal of guidance, control, and dynamics*, 31:81–93, 2008.